***Manuscript**

Probing the sorption reactivity of the edge surfaces in birnessite nanoparticles using nickel(II)

Anna A. Simanova[1], Kideok D. Kwon[2], Sharon E. Bone[3], John R. Bargar[3], Keith Refson[4], Garrison Sposito[5], Jasquelin Peña[1*]

[1] Institute of Earth Surface Dynamics, University of Lausanne, CH-1015 Lausanne, Switzerland

[2] Department of Geology, Kangwon National University, Chuncheon 200-701, Korea

[3] Chemistry and Catalysis Division, Stanford Synchrotron Radiation Lightsource, Menlo Park, California 94025, United States

[4] STFC Rutherford Appleton Laboratory, Didcot, Oxfordshire OX11 0QX, United Kingdom

[5] Geochemistry Department, Earth Sciences Division, Lawrence Berkeley National Laboratory, Berkeley, California 97420 USA

[*] Corresponding author. E-mail: jasquelin.pena@unil.ch; Tel: +47216924355; 4879 Geopolis, UNIL-Mouline, CH-1015 Lausanne

Abstract

Birnessite minerals are layer-type manganese oxides characterized by large surface areas, the presence of cation vacancy sites and varying amounts of structural and adsorbed Mn(III). In this study, we identify the conditions that favor trace metal adsorption on the edge surfaces of birnessite nanoparticles by using Ni as a probe ion for Ni K-edge extended X-ray absorption fine structure (EXAFS) spectroscopy and geometry optimizations based on density function theory (DFT). In δ-MnO_2 nanoparticles free of Mn(II,III) at pH 6.6, Ni was adsorbed primarily at vacancy sites, with a minor fraction of Ni present as a double-edge sharing (DES) or a double-corner sharing (DCS) complex at surface loadings exceeding the vacancy content. In Mn(III)-rich δ-MnO_2 nanoparticles, about 80 % of the adsorbed Ni formed a mixture of DES and DCS complexes at particle edges in samples with loadings ranging from 0.01 to 0.08 mol Ni mol^{-1} Mn, with only a small fraction of vacancy sites available to adsorb Ni. The presence of Mn(III) at the nanoparticle edges also changed the architecture of the DES complex, causing the Ni octahedra to adsorb onto the cavity formed between two Mn(III) octahedra at the particle edges. The EXAFS-derived Ni-Mn interatomic distances of 3.01 – 3.05 Å for this "flipped" Ni-DES complex were in excellent agreement with those obtained by DFT geometry optimization. Edge surfaces on birnessite nanoparticles have a lower affinity for trace metals than vacancy sites, but have a moderate sorption capacity (ca. 0.14 mol Ni mol^{-1} Mn at vacancies *vs.* 0.06 mol Ni mol^{-1} Mn at edge surfaces). Finally, although Mn(III) increases the relative proportion of Ni adsorbed at particle edges by blocking sorption sites on the basal surface, the overall sorption capacity of the mineral diminishes significantly.

1. INTRODUCTION

Birnessite (layer-type MnO_2) minerals undergo strong adsorption reactions with trace metals due to their large specific surface area and negative surface charge (Post, 1999; Tebo et al., 2004). Cation vacancies in the MnO_2 sheet, Mn(III) substitution for Mn(IV), and undercoordinated oxygen atoms at particle edges (Bargar et al., 2009; Lanson et al., 2002b; Manceau et al., 2002; Manceau et al., 2013; Villalobos et al., 2006; Zhu et al., 2012) lead to various surface complex configurations for trace metals, as illustrated in **Fig. 1a − d**. Studies on the mechanisms of trace metal sorption by birnessite have focused on the reactivity of the vacancy sites (e.g. Drits et al., 2002; Lanson et al., 2002b; Manceau et al., 2002; Manceau et al., 2007; Peacock, 2009; Peacock and Sherman, 2007; Peña et al., 2010; Toner et al., 2006), with significantly fewer studies addressing the reactivity of particle edges (Kwon et al., 2010; Takahashi et al., 2007; Villalobos et al., 2005; Villalobos et al., 2014; Wang et al., 2012).

Birnessite particles occur typically as stacked sheets that extend only a few nanometers along the sheet-stacking direction (ca. 1 - 4 nm) and in the *ab* plane (ca. 2 – 10 nm) (Bargar et al., 2009; Lanson et al., 2008; Manceau et al., 2013; Villalobos et al., 2006). Because the proportion of sorption sites at particle edges increases with increasing specific surface area, the edge surfaces of these nanoparticles can contribute significantly to trace metal sorption. Villalobos et al. (2005) found a linear correlation between Pb surface excess and specific surface area, with an analysis of extended X-ray absorption fine structure (EXAFS) spectra indicating that 50 – 75 % of adsorbed Pb was located at particle edges.

The presence of Mn(III) also may influence the extent to which particle edges participate in trace metal sorption reactions. Recent structural models for δ-MnO_2, a synthetic analog of

natural birnessite, include 0.05 to 0.30 mol Mn(III) mol^{-1} Mn incorporated into the MnO_2 sheet or adsorbed above and below vacancy sites (Grangeon et al., 2008; Manceau et al., 2013; Zhu et al., 2012). Based on wet chemistry data, Wang et al. (2012) suggested that the relative contribution of edge sites to trace metal sorption increased as the Mn(III) content increased. The adsorption of Mn(III) at vacancy sites could render these sites less available to adsorb other metals, thus forcing increased trace metal sorption at particle edges. Furthermore, the presence of Mn(III) may influence the structural parameters of surface complexes on birnessite edge sites because the radius of Mn(III) (0.645 Å) is larger than that of Mn(IV) (0.53 Å).

Metals adsorbed on the edge surfaces of hexagonal birnessite have been reported to exhibit two coordination geometries: double-corner-sharing (DCS, **Fig. 1c**) and double-edge-sharing (DES, **Fig. 1d**). Both DCS and DES surface complexes have been proposed for Pb based on EXAFS spectroscopy (Takahashi et al., 2007; Villalobos et al., 2005). However, geometry optimizations based on density functional theory (DFT) (Kwon et al., 2010) show that DES is the preferred coordination for Pb, but the protonation of the mineral surface and the hydration state of the adsorbing metal cation can influence the adsorbate structure. For Ni sorption on hexagonal birnessite, only the DCS species has been reported (Manceau et al., 2007; Yin et al., 2012). The Ni-DCS species was inferred from a decrease in the number of Mn neighbors near 3.5 Å, the interatomic distance diagnostic of triple-corner-sharing surface complexes at vacancy sites (TCS, **Fig. 1a**). Overlap in the metal-Mn interatomic distance of DCS and TCS complexes has been observed for geometry-optimized Pb surface complexes (Kwon et al., 2010). If structural parameters for surface complexes at particle edges overlap with those for surface complexes at vacancy sites, it becomes difficult to assign the coordination geometry based on interatomic distances alone.

In the current study, we aim to clarify the mechanisms of trace metal sorption at particle edges on hexagonal birnessite. Of the trace metals of interest, including Fe, Co, Ni, Cu, Zn and Pb, only Ni is both redox-inactive and shows only symmetric octahedral coordination. These chemical properties facilitate the interpretation of spectroscopic data, thus making Ni the probe metal of choice for this study. We follow a synergistic experimental-computational approach that combines chemical measurements, EXAFS spectroscopy, and DFT geometry optimizations to investigate the mechanisms of Ni sorption by δ-MnO_2, a Mn(III)-rich δ-MnO_2, and triclinic birnessite at pH 6.6. The large specific surface area of δ-MnO_2 provides ample edge surfaces for metal sorption, whereas the Mn(III)-rich δ-MnO_2 sample allowed us to examine the role of Mn(III) without a major change in specific surface area, unlike previous studies (Wang et al., 2012; Villalobos et al., 2014). In addition, using triclinic birnessite (TcBi) as a sorbent, we could compare the structure of Ni surface complexes in a Mn(III)-rich birnessite which has no vacancy sites (Lanson et al., 2002a). We used EXAFS spectroscopy to probe the average bonding environment of Ni and estimate its distribution between different surface sites. The DFT calculations allowed us to determine the structural parameters for variety of surface complexes at the edges and to investigate the effects of protonation and Mn(III) on their structural parameters, which in turn helped to constrain our interpretation of the Ni K-edge EXAFS spectra.

2. MATERIALS AND METHODS

2.1. Materials

All solutions were prepared using ultrapure water with a resistivity of 18.2 MΩ·cm (LaboStar, Siemens) and A.C.S. reagent-grade chemicals. The synthesis and characterization of

the δ-MnO_2 powder used in this study is described elsewhere (Duckworth and Sposito, 2007). Synthetic δ-MnO_2 may have varying amounts of lower-valent Mn in its structure, resulting in an average manganese oxidation number (AMON) < 4.0 that can arise from synthesis conditions (Wang et al., 2012), solution pH (Manceau et al., 2013), or aging of the mineral in aqueous suspension (Villalobos et al., 2003). In this study, we equilibrated δ-MnO_2 (AMON = 4.01 ± 0.05) in a 10 mM NaCl and 10 mM HEPES buffer solution to produce a Mn(III)-rich δ-MnO_2 with AMON = 3.65 ± 0.05. The fractions of Mn(II) and Mn(III) in the solid were determined to be 2 ± 1 % and 34 ± 1 %, respectively, using pyrophosphate extractions (see Electronic Annex). Although HEPES belongs to the Good's buffers that are considered inert and thus widely used to control pH (Good et al., 1966), the piperazine-ring group in the HEPES molecule can act as an electron donor to Mn(IV) (Buchholz et al., 2011; Grady et al., 1988; Kirsch et al., 1998; Zhao and Chasteen, 2006) and lead to the accumulation of Mn(III) in δ-MnO_2. The structural characteristics of this modified δ-MnO_2, which we denote as Mn^{III}_δ-MnO_2, are discussed in the **Electronic Annex**. Triclinic birnessite (TcBi) was synthesized by oxidation of Mn^{2+} at pH 8 (Drits et al., 1997; Giovanoli et al., 1970), since at this alkaline pH, no vacancy sites are expected to form (Drits et al., 1997; Silvester et al., 1997). The properties of our unmodified Mn oxide samples (**Table 1**) compare well with available literature data (Drits et al., 1997; Villalobos et al., 2003; Yang and Wang, 2001). The Mn oxides were stored as dry powders at 4 °C or -20 °C.

2.2. Sorption experiments

Sorption experiments with δ-MnO_2 and Mn^{III}_δ-MnO_2 were conducted at pH 6.6, with pH maintained constant using a pH STAT (Metrohm) or HEPES buffer (Fisher Scientific). The

δ-MnO_2 powder was ground using an agate mortar and pestle and resuspended in either 10 mM NaCl (for sorption experiments on δ-MnO_2) or 10 mM NaCl and 10 mM HEPES buffer (for sorption experiments on Mn^{III}_δ-MnO_2) to achieve a total Mn concentration of 5.7 mM. The mineral suspension was sonicated for one hour (Bransonic 3510 Ultrasonic Cleaner). For pH-STAT experiments (δ-MnO_2), after sonication, 80 mL of the suspension were transferred to a titration vessel on a stir plate and the pH was adjusted to 6.6 by addition of 50 mM HCl. The mineral suspension was equilibrated at pH 6.6 for 30 – 60 min, after which an aliquot of 40 mM $NiCl_2$ was added to achieve an initial Ni concentration between 0 and 1400 μM. In all experiments, the Ni concentrations were below the solubility limit of α-$Ni(OH)_2$. After Ni addition, the suspension pH dropped to about pH 5.5; the pH was re-adjusted using 50 mM NaOH and maintained at pH 6.6 for 48 h. For the HEPES-buffered experiments (Mn^{III}_δ-MnO_2), after sonication, 12 mL of the mineral suspension was transferred from a stock suspension under vigorous stirring to 15-mL polypropylene Falcon tubes. An aliquot of a 10 or 40 mM $NiCl_2$ solution was added to each of 30 tubes to achieve initial Ni concentrations between 0 and 1400 μM. All tubes were placed on an end-over-end shaker (Enviro-Genie, Scientific Industries, Inc.) for 48 h at 35 rpm. Finally, to ensure that HEPES did not modify the sorption of Ni by Mn^{III}_δ-MnO_2, we conducted additional control experiments using Mn^{III}_δ-MnO_2 without HEPES in the background electrolyte. To initiate these experiments, δ-MnO_2 was equilibrated with HEPES for one hour. The Mn^{III}_δ-MnO_2 solids were collected by filtration and resuspended in 10 mM NaCl; the suspension pH was adjusted to 6.6 and maintained constant on a pH-STAT during the Ni sorption reaction.

After 48 h of equilibration, two samples were collected to determine total and aqueous metal concentrations. One milliliter of the suspension was digested with 9 mL of 1.5 % HNO_3

and 10 mM oxalic acid for analysis of total Mn and Ni concentrations (c_{MnTOT} and c_{NiTOT}). The remaining slurry was filtered through a 0.22 μm syringe filter (Millipore). The pH of the filtrate was measured using an Orion A111 pH meter (ThermoScientific) and a semi-micro combination glass pH electrode (Orion Ross, ThermoScientific). The filtrate was then acidified with HNO_3 for analysis of aqueous Mn and Ni concentrations (c_{Mn} and c_{Ni}). The empty test tubes were rinsed first with 5 - 10 mL ultrapure water and then with 5 mL of 1.5 % HNO_3 and 10 mM oxalic acid. Both rinse solutions were analyzed for Ni and Mn concentrations to test whether any Ni or Mn was retained on the tube walls.

Metal concentrations were measured by inductively coupled plasma optical emission spectrometry (ICP-OES, Perkin-Elmer Optima 8300) in triplicate using one to three emission lines per element. Nine standard solutions in the range 0.5 to 500 μM were prepared from 1000 mg/L Perkin-Elmer single element standards. Measured intensities were corrected relative to the intensity obtained from a 50 ppm Sc internal standard. The surface excess of Ni (q) was calculated as $(c_{NiTOT} - c_{Ni})/(c_{MnTOT} - c_{Mn})$ in units of mol Ni mol^{-1} Mn (Peña et al., 2010). Control experiments showed that at most 2 – 4 % of the total Mn was bound to test tube walls; surface excess values of Ni in this fraction corresponded to the Ni surface excess values in the slurry. Thus, we concluded that this small loss of Mn oxide to the tube walls did not influence any trends in our results. Finally, identical surface excess values were measured with and without HEPES in the background electrolyte (data not shown).

2.3. Average Mn oxidation number determination

Average Mn oxidation numbers (AMON) were determined by a three-step potentiometric titration (Metrohm 888 Titrando) that yields a concentration-independent measure of average Mn

oxidation number (Grangeon et al., 2012; Lingane and Karplus, 1946; Vetter and Jaeger, 1966). In Step 1, a 0.02 M Mohr's salt [$(NH_4)_2Fe(SO_4)_2$] solution is titrated with 0.02 M $KMnO_4$. In Step 2, Step 1 is repeated after reductive dissolution of the Mn oxide in a second aliquot of the Mohr's salt solution, where the volumes of Mohr's salt solution in Steps 1 and 2 must be identical. The moles of Fe(II) consumed by Mn(IV,III) reduction to Mn(II) are determined by difference of the $KMnO_4$ volumes used in Steps 1 and 2. In Step 3, the total moles of Mn(II) is determined by back-titration of the solution obtained at the end of Step 2 using 0.02 M $KMnO_4$ in excess Na pyrophosphate (PP) to trap Mn as Mn(III)-PP.

Samples for AMON determination were obtained by filtration. About 37 mL of the mineral suspension (See **Section 2.2**) were passed through a 0.45 μm filter membrane (Millipore). The solid was washed with 30 mL of ultrapure water to remove any entrained ions. The filter membrane was transferred into a titration flask with 40 mL of 0.02 M Mohr's salt solution. For unreacted Mn oxide powders (δ-MnO_2 and TcBi), 40 mg mineral were dissolved in Mohr's salt solution. The AMON values in Table 1 are reported as the mean and standard deviation of triplicate measurements; the standard deviations ranged from ±0.04 to ±0.05, which is consistent with the uncertainties reported previously for this method (Grangeon et al., 2012). The AMON values of unreacted (dry) and wet δ-MnO_2 were both close to 4.0, indicating that neither the filter membrane nor residual water influenced the determination of the AMON.

2.4. X-ray absorption spectroscopy

Samples used for XAS, prepared as described in **Section 2.2**, are listed in **Table 2**. Nickel surface loadings were selected to span the 6 to 11 % (mol vacancy mol^{-1} Mn) range in vacancy content reported for δ-MnO_2 (Manceau et al., 2013; Villalobos et al., 2003). For all samples

196 investigated by XAS, an aliquot of the mineral suspension was collected onto a Millipore filter
197 membrane (ca. 4 mg cm^{-2}). Filter membranes were attached to an Al sample holder and covered
198 with Kapton tape.

199 X-ray absorption spectra were collected at beam lines 4-1 and 11-2 (beam energy 3 GeV,
200 current 450 – 500 mA) of the Stanford Synchrotron Radiation Lightsource using a Si(220) ϕ =
201 90° double crystal monochromator. The vertical slit size was set to 1 mm. The monochromator
202 energy was calibrated using a Ni foil by setting the first inflection point in the first derivative to
203 8333 eV. The incident beam was detuned to 70 % at 10 keV to minimize higher-order
204 harmonics. Sample holders were positioned at a 45° angle to the incident beam. Nickel K-edge
205 spectra were collected in fluorescence mode using a 30-element Ge detector or Lytle detector
206 filled with Ar gas and equipped with soller slits and a Co(III) foil as fluorescent filter. All X-ray
207 absorption spectra were acquired at 77 K (liquid nitrogen cryostat), with three to seven scans
208 collected per sample.

209 Data reduction and analysis of X-ray absorption spectra were performed in SIXPACK
210 (Webb, 2005), which is built on the IFEFFIT engine (Newville, 2001). Replicate scans were
211 aligned to a common energy scale and averaged. The averaged X-ray absorption spectra were
212 background-subtracted and normalized by fitting the pre-edge region using a Gaussian function
213 and the post-edge region using a quadratic function, with E_0 = 8347 eV, R_{bkg} = 1.0 Å, no clamps,
214 *k*-weight = 3. The normalized k^3-weighted EXAFS spectra were Fourier-transformed over a *k*-
215 range of 3 – 11.6 $Å^{-1}$ using a Kaiser-Bessel apodization window with dk = 3 $Å^{-1}$.

216 Nickel K-edge EXAFS spectra were fitted in *R*-space to determine structural parameters
217 for Ni surface complexes. Single- and multiple-scattering paths used for shell-by-shell fitting

were created using the FEFF6L code (Rehr et al., 1991). Crystal Maker (version 2.1.5, CrystalMaker Software Ltd.) was used to visualize different Ni coordination environments and obtain the atomic coordinates for the FEFF input files. The Ni-MnO_2 clusters were based on the crystal structure of hexagonal birnessite (Lanson et al., 2002a). The amplitude reduction factor (S_0^2) was 0.96 in all fits (Peña et al., 2010). All interatomic distances (R) were floated, while different fitting constraints were applied to determine coordination numbers (CNs) and Debye-Waller factors (σ^2).

In general, the EXAFS spectra were fit between 1 and 3.5 Å using three shells: Ni-O, Ni-Mn^{ES}, and Ni-Mn^{CS}. We used Ni-ES to denote any edge-sharing Ni surface complex (i.e., Ni incorporated at the vacancies [Ni-INC] and at the edges [Ni-DES]; **Figs. 1b and 1d**) and Ni-CS to denote any corner-sharing complex (i.e., Ni-TCS at the vacancies and Ni-DCS at the edges; **Figs. 1a and 1c**) because the structural parameters for surface complexes at particle edges may overlap with those for surface complexes at vacancy sites. To avoid *a priori* assignments of coordination geometries, we performed various fits with the CN of each Ni-Mn shell fixed to values between 2 and 6 under the assumptions that Ni adsorbed at particle edges has two Mn neighbors (CN = 2), Ni adsorbed at a vacancy site has six Mn neighbors (CN = 6), and Ni adsorbed in equal proportions between edges and vacancy sites displays an average CN = 4 (**Tables EA1, EA2**). Then, to estimate the fraction of Ni in CS versus ES configurations, we defined the amplitudes (A) of the ES and CS Ni-Mn shells as $CN * f$ and $CN * (1- f)$, where the CNs were constrained to varying values and f represents a species abundance scaling parameter. Finally, the σ^2 values of the ES and CS shells were linked to each other (Peña et al., 2010) in fits to δ-MnO_2 samples, but were both allowed to vary in fits to Mn^{III}_δ-MnO_2 samples, which contained significant proportions of Mn(III) in the structure. Due to large difference in the ionic

radii of Mn(III) or Mn(IV) atoms (i.e. 0.645 and 0.53 Å, respectively), the σ^2 values of the metal-Mn shells in the CS and ES complexes may differ significantly depending on metal coordination to Mn(III) or Mn(IV).

The fitting routine described above resulted in a large number of fits. In order to determine which fits were most plausible, we evaluated 1) whether the amplitudes of the Ni-Mn shells were consistent with a high or low number of Mn neighbors; 2) how well the σ^2 value compared to values reported in the literature; and 3) the probability (α') that a fit with R-factor R_i represented a statistically better fit (> 60 %) than the fit with the lowest R-factor, following the Hamilton test (Calvin, 2013; Downward et al., 2006).

2.5. Geometry optimizations

Model Ni surface complexes for geometry optimization were constructed using a 1 nm nanodisk consisting of seven Mn(IV) octahedra (**Fig. 2**). For DCS species, Ni was initially bound to two singly-coordinated O (O_{1Mn}) at the nanodisk lateral edge and four H_2O molecules to achieve a coordination number of six. For DES species, Ni was initially bound either to one doubly-coordinated O (O_{2Mn}) or one triply-coordinated O (O_{3Mn}) along with two singly-coordinated O (O_{1Mn}) and three H_2O molecules to achieve a coordination number of six (e.g., DES_{O2Mn} or DES_{O3Mn}). We also geometry optimized an edge-sharing species wherein Ni binds to three Mn octahedra via two singly- and two doubly-coordinated O (ES in **Fig. 2**). Dangling Mn-O bonds at particle edges were charge-balanced with one or two protons, yielding surface Mn-OH or Mn-OH_2 and an overall model structural formula, $Mn_7NiO_xH_y$ (x = 27 – 28, y = 24 – 26), depending on surface complex type. Based on Pauling's second rule and magnetic moment

262 calculations (Kwon et al., 2010), the bridging O_{1Mn} between Mn and Ni is protonated (i.e. Mn-
263 OH-Ni) (**Fig. 2**).

264 To investigate the effect of Mn(III) on the structural parameters of Ni-DES complexes,
265 we replaced one or two Mn(IV) octahedra at the nanodisk edge with Mn(III) and geometry-
266 optimized the structures, $DES_{O2Mn}^{1Mn(III)}$, $DES_{O3Mn}^{1Mn(III)}$, and $DES_{O3Mn}^{2Mn(III)}$. When both Mn(IV) octahedra
267 were replaced with Mn(III) octahedra to form $DES_{O2Mn}^{2Mn(III)}$, we were unable to obtain a stable
268 geometry-optimized structure because Mn(III) transformed to a different oxidation state, as
269 indicated by the calculated magnetic moment size. Thus we considered the $DES_{O2Mn}^{2Mn(III)}$ species
270 unstable.

271 Model Ni-MnO_2 structures were geometry-optimized using CASTEP, a planewave
272 periodic DFT code (Clark et al., 2005) with the spin-polarized generalized gradient
273 approximation functional GGA/PBE (Perdew et al., 1996) and ultrasoft pseudopotentials
274 (Vanderbilt, 1990). The kinetic energy cutoff was 500 eV. To minimize spurious interactions
275 between structural models of periodic cells, a sufficiently large simulation cell size of 20 Å x 20
276 Å x 16 Å was used so that the model converged well with respect to structural parameters (Kwon
277 et al., 2010). Geometry optimizations were carried out at one *k*-point at (0.0, 0.0, 0.0) under the
278 BFGS procedure (Pfrommer et al., 1997) by relaxing all atoms of the surface complex in the
279 fixed periodic cell. The energy tolerance was 5 x 10^{-6} eV/atom. The maximum tolerance for
280 force and atom displacement along any Cartesian component was 0.03 eV/Å and 0.001 Å,
281 respectively. The magnetic ordering was ferromagnetic among Mn ions but antiferromagnetic
282 between Ni and Mn ions. The geometry-optimized structures in **Fig. 2** were visualized using the
283 VESTA software (Momma and Izumi, 2011).

In geometry optimizations of the Mn(III)-rich nanodisk, we used the DFT + U formalism which adds the on-site coulomb interaction *U*, a Hubbard term, to the DFT total energy because standard DFT tends to over-delocalize the 3*d* electrons in Mn oxides (Anisimov et al., 1997; Franchini et al., 2007; Rollmann et al., 2004). In CASTEP, the DFT + U formalism is implemented with a rotationally-invariant model (Cococcioni and de Gironcoli, 2005; Dudarev et al., 1998), which uses an effective Hubbard term ($U_{eff} = U - J$, where J is an intra-exchange term). We used U_{eff} = 2.5 eV only for the 3*d* orbitals of Mn(III) in the nanodisk. The calculated magnetic moment of Mn(III) was 4.1 μ_B (μ_B is the Bohr magneton) while that of Mn(IV) was 2.9 – 3.0 μ_B. The choice of U_{eff} = 2.5 eV was validated based on the Mn-3*s* exchange splitting energy (ΔE_{3s}), which correlates strongly with the Mn oxidation state (Oh et al., 1992). For example, ΔE_{3s} for Mn(IV) is 3.3 eV in the Mn(IV) nanodisk, while that for Mn(III) in LiMn(III)O_2 and PbMn(III)O_2OH (quenselite) is 4.7 – 4.8 eV (Kwon et al., 2010). In the Mn(III)-rich nanodisk, ΔE_{3s} for Mn(III) was 5.0 eV, very close to the values for LiMn(III)O_2 and PbMn(III)O_2OH.

3. RESULTS

3.1. Nickel sorption isotherms

Nickel sorption isotherms for δ-MnO_2 and Mn^{III}_δ-MnO_2 at pH 6.6 are shown in **Fig. 3**. Sorption by δ-MnO_2 followed an H-type isotherm, whereas for Mn^{III}_δ-MnO_2 it followed an L-type isotherm (Sposito, 2008). For these latter Ni sorption data, a maximum surface excess equal to 0.14 ± 0.05 mol Ni mol^{-1} Mn was estimated from a plot of the distribution coefficient ($K_d = q / c$) against surface excess (q) (Sposito, 2008).

In Ni sorption experiments with δ-MnO_2, no aqueous Mn(II) was detected at the end of the sorption reaction and no change was measured in the AMON value of the solid phase (**Table**

306 **2**). By contrast, Ni sorption by Mn^{III}_δ-MnO_2 was accompanied by the accumulation of Mn(II)
307 in solution (**Fig. EA4**). At loadings below 0.04 mol Ni mol^{-1} Mn, only 4 – 5 μM Mn was
308 released in solution. As the Ni loading increased from 0.04 to 0.13 mol Ni mol^{-1} Mn, Mn(II) in
309 solution increased linearly, reaching a maximum of 3.5 % of the total Mn concentration (**Fig.**
310 **EA4**). The amounts of Mn(II) measured in solution correspond to an increase in the AMON of
311 the solid phase by 0.04 – 0.08, which is in agreement with the increase in measured AMON of
312 3.68 to 3.73 as the Ni loading increased from 0.01 to 0.08 mol Ni mol^{-1} Mn (**Table 2**). In
313 addition, the amount of Mn(II) released to the aqueous phase upon Ni sorption is consistent with
314 the amount of Mn(II) (2 ± 1 %) initially sorbed at the surface of Mn^{III}_δ-MnO_2. The linear
315 relationship between the amounts of sorbed Ni and Mn(II) released at Ni surface loadings > 0.04
316 mol Ni mol^{-1} Mn (**Fig. EA4**) suggests that Ni and Mn(II) compete for the same surface sites
317 (Murray, 1975; Peña et al., 2010).

318 **3.2. Ni K-edge EXAFS spectra**

319 *3.2.1. Coordination environment of Ni sorbed by δ-MnO_2*

320 Nickel K-edge EXAFS spectra and the corresponding Fourier transforms for δ-MnO_2
321 equilibrated with Ni are presented in **Fig. 4**. The Fourier transforms show three dominant peaks
322 at 1.6, 2.4, and 3.1 Å (*R* + *dR*), representing Ni-O, Ni-Mn, and Ni-Mn shells, respectively. The
323 peak at 2.4 Å (*R* + *dR*) is usually assigned to the first Ni-Mn shell for the Ni-INC species, while
324 the peak at 3.1 Å (*R* + *dR*) is usually assigned to the first Ni-Mn shell for the Ni-TCS species
325 (Manceau et al., 2007; Peacock and Sherman, 2007; Peña et al., 2010). In sample Ni 0.05, the
326 amplitude of the CS shell was comparable to the amplitude of the Ni-Mn shell in samples with
327 Ni sorbed dominantly at vacancy sites (Peña et al., 2010), while in sample Ni 0.18, the amplitude

of the CS shell was reduced by about 40 %. Thus, in our shell-by-shell fits (**Table EA1**) we excluded the possibility of a significant contribution from DCS species (low CNs) in Ni 0.05 and TCS species (high CNs) in Ni 0.18 (Manceau et al., 2007; Peña et al., 2010; Zhu et al., 2010b). All shell-by-shell fits returned a Ni-Mn^{ES} distance of 2.84 – 2.91 (± 0.01) Å and a Ni-Mn^{CS} distance of 3.47 ± 0.01 Å (Table 3). At low loadings (Ni 0.05), the best fits were obtained when the *CN* of the Ni-Mn^{CS} and Ni-Mn^{ES} shells were set equal to 6. At high loadings (Ni 0.18), statistically-similar fit results were obtained when the *CN* of the Ni-Mn^{CS} shell was set equal to 5 or 6 and the *CN* of the Ni-Mn^{ES} shell was set equal to values between 3 and 6 (**Table EA1**).

In **Table 3** we report the fitting parameters for Ni 0.05 for the scenario in which Ni binds at vacancy sites as either Ni-TCS or Ni-INC species, with the CN equal to 6 for each Ni-Mn shell (**Figs. 4 and EA5**). For the high loading sample (Ni 0.18), we report the fitting parameters for the scenarios where a moderate proportion of Ni binds at particle edges either in DES or DCS geometries by setting the corresponding *CN* of the Ni-Mn shells equal to 4 or 5 (**Table 3**). The final fits included two additional shells (i.e., Ni-O_3 and Ni-Mn_2^{CS}) to account for longer-distance Ni-O/Mn pair correlations corresponding to the TCS species (Peña et al., 2010). The fitted Debye-Waller factors of the first Ni-Mn^{CS} shell were in the range 0.007 – 0.010 $Å^{-1}$, which is comparable to the values previously reported for Ni-CS species on birnessite (Manceau et al., 2007; Peña et al., 2010; Zhu et al., 2010b). Based on the fitted values of *f* (**Table 3**), we conclude that CS complexes represent 80 – 87 % of the total adsorbed Ni at both surface loadings. Using the relationship $q_{Ni\text{-}CS} = q * f$, we estimate approximately 0.04 and 0.15 mol Ni mol^{-1} Mn in the CS geometry for samples Ni 0.05 and Ni 0.18, respectively. The uncertainty in the fitted parameter, *f*, and thus Ni speciation, ranged from 2 to 4 %. However, we assign a 20 % uncertainty to these Ni speciation estimates to be consistent with typical uncertainties associated

with coordination numbers. Although the amount of the ES species is small (0.01 – 0.04 mol Ni mol^{-1} Mn), the presence of a small but real fraction of Ni-Mn^{ES} species is supported by significant improvement in the fit statistics upon addition of the Ni-Mn^{ES} to the fit (R-factor decreased from 0.046 to 0.013).

3.2.2 Coordination environment of Ni sorbed by Mn^{III}_δ-MnO_2

Nickel K-edge EXAFS spectra and corresponding Fourier transforms for Mn^{III}_δ-MnO_2 equilibrated with Ni are shown in **Fig. 5 and EA6**. The Fourier transforms have dominant peaks at 1.6, 2.5, and 3.1 Å (*R* + *dR*) due to Ni-O, Ni-Mn, and Ni-Mn scattering, respectively. The Ni-Mn shells are at positions similar to those observed for the δ-MnO_2 samples, but the first Ni-Mn peak appears shifted, from 2.4 Å to 2.5 Å (*R* + *dR*). This peak is best-resolved for the sample with the lowest Ni loading, which shows the least peak overlap between the two Ni-Mn shells. Finally, in contrast to the Fourier-transformed EXAFS spectra for the δ-MnO_2 samples, the Fourier-transformed EXAFS spectra for Mn^{III}_δ-MnO_2 show no structure for *R* + *dR* > 4 Å.

Fits to the EXAFS spectra from the Mn^{III}_δ-MnO_2 samples resulted in interatomic distances of 2.04 ± 0.01 Å, 3.05 ± 0.03 Å and 3.47 ± 0.02 Å for the Ni-O, Ni-Mn^{ES} and Ni-Mn^{CS}, respectively (**Table 4**). The Ni-Mn^{CS} distance is identical to that obtained for Ni sorbed on δ-MnO_2. However, the Ni-Mn^{ES} distance is longer by 0.18 Å than the Ni-Mn^{ES} distance for δ-MnO_2, but it is similar to the Ni-Mn distance reported for the Ni complexes at the edge sites in triclinic birnessite (Peacock and Sherman, 2007; Zhu et al., 2010b). Indeed, the Fourier-transformed EXAFS spectrum for our TcBi sample showed a major second-shell peak at 2.5 Å (*R* + *dR*), which was fit well with 3.2 ± 0.45 Mn atoms at 3.09 ± 0.01 Å (**Table 4, Figs. 5 and**

372 **EA7**). Thus, the observed elongation of the Ni-Mn^{ES} distance in Mn^{III}_δ-MnO_2 is consistent with
373 coordination of Ni to Mn(III) octahedra in the ES configuration.

374 In the shell-by-shell fits, the scenario where CS species form exclusively at the vacancy
375 sites [*CN*(Ni-Mn^{CS})=6] resulted in an unreasonably high Debye-Waller factor (>0.025 $Å^2$) and
376 thus was excluded. The absence of a significant fraction of Ni-TCS species is also supported by
377 the amplitudes of the Ni-Mn^{CS} shell, as well as the higher-order shells, which are significantly
378 attenuated relative to those of the δ-MnO_2 samples. Moreover, since Mn^{III}_δ-MnO_2 has both
379 Mn(III) and Mn(IV) atoms, the σ^2 values of the ES species were expected to exhibit higher
380 values than in δ-MnO_2 due to higher disorder in interatomic distances and thus σ^2 values of
381 0.014 $Å^{-1}$ (twice as large in δ-MnO_2) or lower were considered as reasonable. In samples Ni 0.01
382 and Ni 0.04, shell-by-shell fits with *CN*(Ni-Mn^{ES}) and *CN*(Ni-Mn^{CS}) set equal to 2 - 3 and 3 – 4,
383 respectively, returned statistically-similar results. In **Table 4** and **Figs. 5** and **EA6** we report the
384 fits obtained with *CN*(Ni-Mn^{ES}) = 2 and *CN*(Ni-Mn^{CS}) = 4. The σ^2 values were 0.009 – 0.012 $Å^{-1}$
385 for the Ni-Mn^{ES} shell and 0.006 – 0.007 $Å^{-1}$ for the Ni-Mn^{CS} shell, which are consistent with the
386 values reported for Ni-MnO_2 surface complexes (Manceau et al., 2007; Peña et al., 2010; Zhu et
387 al., 2010b). The fits indicate a mixture of Ni-ES and Ni-CS complexes at all surface loadings
388 studied: 39 – 61 % Ni-ES ($q_{Ni\text{-}ES}$ = 0.005 – 0.049 mol Ni mol^{-1} Mn) and 61 – 39 % Ni-CS ($q_{Ni\text{-}CS}$
389 = 0.005 – 0.031 mol Ni mol^{-1} Mn, with an uncertainty of 20 - 29 % as determined from the
390 uncertainty in *f*.

391 **3.3. Geometry optimizations of Ni edge surface species**

392 Geometry-optimized structures of Ni edge surface species are summarized in **Fig. 2** and
393 **Table 5**. Overall, the average Ni-O distance [*d*(Ni-O)] ranges from 2.08 – 2.11 Å for all model

surface complexes. Our geometry optimizations also show significant overlap in *d*(Ni-Mn) obtained for surface complexes with similar connectivity between the Ni and Mn octahedra (**Table 5**). For example, the value of *d*(Ni-Mn) for Ni-DCS (**Table 5**) is within 0.02 Å of *d*(Ni-Mn) for Ni-TCS (**Table 3**). Thus, Ni-DCS cannot be distinguished experimentally from Ni-TCS based solely on the Ni-Mn interatomic distance. In addition, the protonation of the doubly coordinated oxygen atom (O_{2Mn}) does not affect *d*(Ni-Mn), as indicated by *d*(Ni-Mn) = 3.45 Å obtained for both the deprotonated (DCS_0) and protonated (DCS_H) DCS structures. Finally, the Ni-Mn distance (2.89 Å) obtained for the Ni-DES complex, where Ni binds to two Mn(IV) octahedra via two doubly-coordinated O (DES_{O2Mn}), is similar to the Ni-Mn distance (2.91 Å) for ES, where Ni binds to three Mn(IV) octahedra, and to the Ni-Mn distance (2.87 Å) reported for Ni-INC, where Ni binds to six Mn(IV) octahedra (Peacock, 2009; Peacock and Sherman, 2007; Peña et al., 2010). Therefore, the INC, DES_{O2Mn} and ES species also cannot be resolved using only *d*(Ni-Mn) (**Fig. 2**).

In geometry optimizations of the nanodisk with Mn(III) octahedra located at the edges, we found that *d*(Ni-Mn) in Ni-DES is sensitive to the valence of the Mn to which Ni is connected by O. In the absence of Mn(III), when Ni is coordinated to two singly-coordinated O and one doubly-coordinated O, forming DES_{O2Mn}, *d*(Ni-Mn) is 2.89 Å. When one of the Mn(IV) octahedra was replaced with a Mn(III) octahedron ($DES_{O2Mn}^{1Mn(III)}$), *d*(Ni-Mn) increased slightly, from 2.89 Å to 2.91 Å. In geometry-optimized DES_{O3Mn} (**Fig. 2**), Ni coordinates to one triply-coordinated O and two singly-coordinated O (i.e., the Ni octahedron "flips" onto the basal plane at the particle edge). When one or two of the Mn(IV) octahedra to which Ni binds were replaced with Mn(III) octahedra to form $DES_{O3Mn}^{1Mn(III)}$ or $DES_{O3Mn}^{2Mn(III)}$, respectively, *d*(Ni-Mn) increased from 2.97 Å to 3.05 Å (**Table 5**). This longer distance, caused by the presence of Mn(III) at the

417 particle edges in $DES_{O3Mn}^{2Mn(III)}$, corresponds well to the experimentally observed Ni-Mn interatomic
418 distance for Ni sorbed on TcBi [*d*(Ni-Mn) = 3.09 Å] and, importantly, to the Ni-Mn interatomic
419 distance observed for Ni sorbed on Mn^{III}_δ-MnO_2 [*d*(Ni-Mn) = 3.01 − 3.05 Å].

420 **4. DISCUSSION**

421 In previous studies, attempts to resolve the role of particle edges in trace metal sorption
422 by birnessite minerals have been limited by i) co-variation in the specific surface area and
423 Mn(III) content of the minerals investigated and ii) a lack of sufficient molecular-scale
424 information to determine the structural parameters of surface complexes formed. In the current
425 study, the hexagonal birnessite minerals used were characterized by large specific surface areas
426 and differing Mn(III) contents. The large specific surface areas provide ample edge surface area
427 for metal sorption, whereas the large differences in Mn(III) content allowed determination of the
428 influence of Mn(III) on Ni sorption mechanisms without confounding effects from varying
429 specific surface area.

430 **4.1. Ni sorption at particle edges of δ-MnO_2**

431 Nickel K-edge EXAFS spectroscopy showed that the particle edges of δ-MnO_2 at pH 6.6
432 become reactive at surface loadings exceeding the vacancy content. At a loading of 0.18 mol Ni
433 mol^{-1} Mn, the sorption of Ni at edge surfaces was suggested by the decreased amplitude of the
434 $Ni\text{-}Mn^{CS}$ shell in the Fourier-transformed EXAFS spectra (**Fig. 4**). Our geometry optimizations
435 showed that the Ni-Mn distance in both Ni-TCS and Ni-DCS structures were for all practical
436 purposes identical. This result is consistent with previous reports for Ni surface complexes
437 (Manceau et al., 2007) and similar surface complexes of Pb on MnO_2 (Kwon et al., 2010). For

438 the fitting scenario with *CN*(Ni-Mn^{CS}) = 5 and *CN*(Ni-Mn^{ES}) = 6 (**Table 3, Figs. 4 and EA5**), the
439 fractions of the ES and CS complexes were 13 % (or 0.02 mol Ni^{ES} mol^{-1} Mn) and 87 % (or 0.16
440 mol Ni^{CS} mol^{-1} Mn), respectively. Assuming that *CN*(Ni-Mn^{TCS}) = 6 and *CN*(Ni-Mn^{DCS}) = 2
441 (**Fig. 1**), we estimate that the DCS complex constitutes 22 % of the adsorbed Ni or 0.04 mol Ni
442 mol^{-1} Mn. The similarity in fitting statistics when the coordination number of the Ni-Mn^{ES} shell
443 was varied from 3 to 6 (**Table EA1**) suggests that Ni-DES_{O2Mn} or Ni-ES_{O2Mn} complexes may
444 form at particle edges, contributing at most 0.02 mol Ni mol^{-1} Mn (or 10 %). Thus, in the high
445 loading sample 80 – 90 % of the adsorbed Ni, or 0.14 ± 0.04 mol Ni mol^{-1} Mn, is sorbed at the
446 vacancies (TCS/INC), while the contribution from edge species is at most 10 – 20 %, or 0.02 -
447 0.04 mol Ni mol^{-1} Mn as DES/ES/DCS. The predominance of Ni surface complexes at the
448 vacancy sites at low loadings and increase in Ni-DCS and Ni-DES species at high loadings is
449 consistent with the high sorption affinity and capacity of δ-MnO_2 for Ni (**Fig. 3**).

450 **4.2. Ni sorption at particle edges of Mn^{III}_δ-MnO_2**

451 For Mn^{III}_δ-MnO_2, shell-by-shell fits showed a mixture of 39 – 61 % Ni-ES and 61 – 39
452 % Ni-CS complexes. The best fits were obtained for *CN*(Ni-Mn^{ES}) equal to 2 - 3 and *CN*(Ni-
453 Mn^{CS}) equal to 3 – 4, which suggest a 75 - 100 % contribution of the DES species to the Ni-
454 Mn^{ES} shell and a 50 - 75 % contribution of the DCS species to the Ni-Mn^{CS} shell. Thus, the
455 analysis of Ni K-edge EXAFS spectra suggested 29 – 61 % Ni-DES and 46 – 20 % of Ni-DCS
456 complexes in samples with loadings of 0.01 – 0.08 mol Ni mol^{-1} Mn, which sums to around 80 %
457 Ni adsorbed at edge surface sites. We estimate that the highest loading sample (Ni 0.08)
458 contained about 0.06 ± 0.02 mol Ni mol^{-1} Mn adsorbed at particle edges. Although the
459 uncertainty in these estimates is relatively large (20 - 29 %), the majority of Ni is sorbed at the
460 particle edges in Mn^{III}_δ-MnO_2 at pH 6.6. The large fraction of Ni edge species in Mn^{III}_δ-MnO_2

461 as compared to δ-MnO_2 can be explained by the blocking effect of interlayer Mn(II,III)
462 occupying the high-affinity vacancy sites (see **Electronic Annex**). This inference is confirmed
463 by the sorption isotherm for Ni on Mn^{III}_δ-MnO_2, which, unlike the H-curve isotherm observed
464 for δ-MnO_2, does not display high affinity and sorption capacity (**Fig. 3**). The proposed blocking
465 mechanism also explains the decrease in metal sorption capacity observed with increasing
466 Mn(II,III) content in previous studies of birnessites (Lafferty et al., 2010; Wang et al., 2012;
467 Zhao et al., 2009).

468 Trivalent Mn at the particle edges of Mn^{III}_δ-MnO_2 also changes the coordination
469 geometry of Ni surface complexes at the edge sites. Structural modeling of the Ni K-edge
470 EXAFS spectra showed that Mn(III) shifted the Ni-Mn^{ES} distance from 2.84 Å in δ-MnO_2 to 3.01
471 – 3.05 Å in Mn^{III}_δ-MnO_2, close to the Ni-Mn distance obtained for TcBi (**Tables 3 and 4**).
472 Thus, we propose that, in Mn^{III}_δ-MnO_2, Ni forms Ni-DES surface complexes wherein the Ni-
473 Mn distance is elongated due to Mn(III) located at the particle edges.

474 Previously, the elongated Ni-Mn distance in TcBi has been also assigned to Ni complexes
475 formed at the edge surface sites on TcBi (Peacock and Sherman, 2007; Zhu et al., 2010b).
476 However, TcBi is a microcrystalline Mn(III)-containing birnessite with a specific surface area of
477 only 30 m^2/g and relatively large particles. For 50 nm square particles, less than 2 % of the total
478 number of Mn octahedra would be located at the particle edges. In addition, the ordering of
479 Mn(III) into Mn(III)-rich rows in TcBi (Drits et al., 1997; Lanson et al., 2002a; Silvester et al.,
480 1997) creates undersaturated triply-coordinated oxygen atoms on the basal plane, thus making
481 the triangular cavity between these oxygen atoms reactive toward metal cation sorption. Rather
482 than forming a DES complex at particle edges, Ni may be adsorbed as a triple-edge sharing
483 (TES) complex on these triangular cavities in the basal plane. This conclusion is consistent with

484 our EXAFS-derived structural parameters, which showed that Ni-ES in TcBi has three Mn
485 neighbors, two of which should be Mn(III). In Mn^{III}_δ-MnO_2, however, the occurrence of the
486 TES complex is unlikely because it would require significant ordering of the Mn(III) in the
487 MnO_2 sheet; such ordering of Mn(III) is not consistent with our Mn K-edge EXAFS spectra.
488 High specific surface area (ca. 200 m^2 g^{-1}) also favors DES over TES complexes in Mn^{III}_δ-
489 MnO_2.

490 The coordination of Ni to Mn(III) at particle edges of Mn^{III}_δ-MnO_2 is further supported
491 by our geometry optimizations, which showed that Mn(III) influenced both the Ni-Mn distance
492 and bonding geometry of the Ni-DES species. In the absence of Mn(III), Ni was coordinated at
493 the edge sites in the DES_{O2Mn} configuration, while the replacement of Mn(IV) with Mn(III)
494 favored the formation of the $DES_{O3Mn}^{2Mn(III)}$ species (**Fig. 2**). The $DES_{O3Mn}^{2Mn(III)}$ coordination geometry
495 is characterized by a Ni-Mn distance of 3.05 Å, which matches the Ni-Mn distance of 3.01 −
496 3.05 Å detected by EXAFS spectroscopy. In this coordination geometry, Ni binds to a triply-
497 coordinated oxygen O_{3Mn} and "flips" onto the basal plane at particle edges. The formation of the
498 "flipped" DES complex can be rationalized by bond-valence analysis. When a triply-coordinated
499 O is bonded to three Mn(IV) (i.e., O_{3Mn} in DES_{O2Mn}), each Mn(IV) brings +4/6 valence units
500 (v.u.) to O_{3Mn} (i.e., 3 × 4/6 = 2), rendering this O_{3Mn} saturated. The substitution of Mn(IV) by
501 Mn(III) (as in $DES_{O3Mn}^{2Mn(III)}$) makes the O_{3Mn} undersaturated (i.e., 4/6 + 2 × 3/6 = 10/6 < 2) and
502 thus reactive towards metal cation sorption. Consequently, when Mn(III) is present at particle
503 edges, Ni may preferentially form a $DES_{O3Mn}^{2Mn(III)}$ complex in which O_{3Mn} becomes saturated (10/6
504 + 2/6 = 2). In addition, the Ni DES_{O3Mn} geometry may result in a more stable complex at the
505 oxide surface than one with the DCS geometry because DES_{O3Mn} binds with one O_{3Mn} and two
506 O_{2Mn}, while DCS binds with only two O_{2Mn} (**Fig. 2**).

5. CONCLUSIONS

In this study we demonstrate that the edge surfaces of hexagonal birnessite nanoparticles are reactive towards trace metal sorption at circumneutral pH values (6.6). In unmodified and modified δ-MnO_2, Ni sorbed at particle edges under conditions where the vacancy sites were unavailable for sorption. For δ-MnO_2, the fraction of Ni on edge sites was 10 to 20 % and represented a low loading (0.02 – 0.04 mol Ni mol^{-1} Mn) relative to the loading of Ni on vacancy sites (ca. 0.14 mol Ni mol^{-1} Mn) and total surface excess (0.18 mol Ni mol^{-1} Mn). For Mn^{III}_δ-MnO_2, sorption at particle edges was significant, accounting for around 80 % of the total sorbed Ni. Moreover, because Mn(II,III) was present initially in the sorbent, Ni partitioned to the particle edges at all surface loadings studied (0.01 – 0.08 mol Ni mol^{-1} Mn).

Based on EXAFS spectroscopy and DFT geometry optimizations, we conclude that the DCS geometry is favored over the DES geometry in δ-MnO_2, whereas DCS and DES complexes are comparably important in Mn^{III}_δ-MnO_2. The presence of Mn(III) at particle edges in Mn^{III}_δ-MnO_2 forced Ni into the $DES^{2Mn(III)}_{O3Mn}$ geometry, thereby stabilizing the DES complex by providing better charge balance and increasing the number of surface oxygens binding Ni from two to three. This Ni-DES species has not been identified in previous studies with δ-MnO_2 or acid birnessite (Peacock and Sherman, 2007; Yin et al., 2012), a result which may be attributed to differences in mineral specific surface area or Mn(III) content and distribution. Similar structural parameters to those we identified for Ni-DES have been reported for Fe sorbed on δ-MnO_2, although the Mn(III) content of the sorbent after reaction with Fe(III)-desferrioxamine B was not reported (Duckworth et al., 2008)

528 The results presented herein and in previous studies (Manceau et al., 2007; Yin et al.,
529 2012) confirm that EXAFS spectroscopy is limited in its ability to distinguish between surface
530 complexes on basal surfaces and edge surfaces because interatomic distances are similar for
531 complexes with similar polyhedral connectivity (e.g., Ni-TCS and Ni-DCS), as shown by our
532 DFT geometry optimizations. In addition, coordination numbers are poorly constrained in the
533 structural analysis of EXAFS spectra (Ravel and Kelly, 2007). Only by combining DFT
534 geometry optimizations and spectroscopic titrations were we able to identify the structural
535 parameters and coordination geometries of Ni edge complexes. In addition, while we expect Ni
536 and other trace metals to behave similarly, the detection of Fe, Co, Cu, Zn or Pb surface
537 complexes at the edges of birnessite would be more difficult due to the varied coordination these
538 metals display. For instance, Zn forms complexes with both tetrahedral and octahedral
539 geometries on MnO_2 (Fuller and Bargar, 2014; Grangeon et al., 2012; Toner et al., 2006), Co
540 shows the +2 and +3 valence states (Manceau et al., 1997), and Cu and Pb deviate from
541 symmetric octahedral coordination (Kwon et al., 2010; Manceau et al., 2002; Takahashi et al.,
542 2007; Villalobos et al., 2005).

543 In summary, the propensity for trace metals to adsorb at particle edges depends on the i)
544 density of edge sorption sites, ii) valence of Mn atoms at the particle edges, which can modify
545 the type of surface complex formed, and iii) abundance of vacancy sites, which are high-affinity
546 sorption sites but can be blocked by Mn(II,III). The blocking effect of Mn(II, III) also leads to a
547 significant reduction in the overall sorption capacity of Mn oxides. Although the density of
548 reactive edge surface sites, vacancy content and sorbed Mn(II,III) is pH dependent (Manceau et
549 al., 2013; Zhu et al., 2010a), thus influencing the overall reactivity of the edge sites, our findings
550 are relevant for a range of natural settings with circumneutral pH. Natural birnessites occur as

nanoparticles characterized by high surface area and varying amounts of Mn(III), which may originate from the incomplete oxidation of Mn(II) to Mn(IV) or from the reduction of Mn(IV) by redox-active metals (e.g., Co(II), Cr(III), As(III), U(IV)), reducing moieties in natural organic matter, organic contaminants or microorganisms. Thus, understanding how Mn(III) influences the partitioning of metals to different binding sites on birnessite furthers our ability to predict the controls that Mn oxides exert on the distribution and bioavailability of trace metals in the environment.

Acknowledgements

This research was funded by the Director, Office of Energy Research, Office of Basic Energy Sciences of the U.S. Department of Energy under Contract No. DEAC02-05CH11231 and a Sandoz Family Foundation Grant to J. Peña. K. Kwon acknowledges support from the Basic Science Research Program through the National Research Foundation of Korea (NRF) funded by the Ministry of Science, ICT and Future Planning (NRF-2013R1A1A1004657). Portions of this research were carried out at the Stanford Synchrotron Radiation Lightsource, a national user facility operated by Stanford University on behalf of the U.S. Department of Energy, Office of Basic Energy Sciences. Parts of our computations were performed by using resources of the National Energy Research Scientific Computing Center, which is supported by the Office of Science of the U.S. Department of Energy under Contract No. DE-AC02-05CH11231. G. Sposito acknowledges support from his appointment as Chancellor's Professor, University of California at Berkeley. Finally, the authors thank Case van Genuchten for the PDF data and Francesco F. Marafatto for the preparation of TcBi.

574 **References**

575 Anisimov, V.I., Aryasetiawan, F., Lichtenstein, A.I. (1997) First-principles calculations of the
576 electronic structure and spectra of strongly correlated systems: The LDA+U method. *Journal of*
577 *Physics-Condensed Matter* **9**, 767-808.

578 Bargar, J.R., Fuller, C.C., Marcus, M.A., Brearley, A.J., Perez De la Rosa, M., Webb, S.M.,
579 Caldwell, W.A. (2009) Structural characterization of terrestrial microbial Mn oxides from Pinal
580 Creek, AZ. *Geochim. Cosmochim. Acta* **73**, 889-910.

581 Buchholz, A., Laskov, C., Haderlein, S.B. (2011) Effects of zwitterionic buffers on sorption of
582 ferrous iron at goethite and its oxidation by CCl4. *Environ. Sci. Technol.* **45**, 3355-3360.

583 Calvin, S. (2013) *XAFS for everyone*. Taylor & Francis.

584 Clark, S.J., Segall, M.D., Pickard, C.J., Hasnip, P.J., Probert, M.J., Refson, K., Payne, M.C.
585 (2005) First principles methods using CASTEP. *Zeitschrift Fur Kristallographie* **220**, 567-570.

586 Cococcioni, M., de Gironcoli, S. (2005) Linear response approach to the calculation of the
587 effective interaction parameters in the LDA+U method. *Physical Review B* **71**, 035105.

588 Downward, L., Booth, C.H., Lukens, W.W., Bridges, F. (2006) A Variation of the F-Test for
589 Determining Statistical Relevance of Particular Parameters in EXAFS Fits. *X-Ray Absorption*
590 *Fine Structure - XAFS13: 13th International Conference. Proceedings held at Stanford,*
591 *California, 9-14 July, 2006. AIP Conference Proceedings Volume 882.* , 129-131.

592 Drits, V.A., Lanson, B., Bougerol-Chaillout, C., Gorshkov, A.I., Manceau, A. (2002) Structure
593 of heavy-metal sorbed birnessite: Part 2. Results from electron diffraction. *American*
594 *Mineralogist* **87**, 1646-1661.

595 Drits, V.A., Silvester, E., Gorshkov, A.I., Manceau, A. (1997) Structure of synthetic monoclinic
596 Na-rich birnessite and hexagonal birnessite .1. Results from X-ray diffraction and selected-area
597 electron diffraction. *American Mineralogist* **82**, 946-961.

598 Duckworth, O.W., Bargar, J.R., Sposito, G. (2008) Sorption of ferric iron from ferrioxamine B to
599 synthetic and biogenic layer type manganese oxides. *Geochim. Cosmochim. Acta* **72**, 3371-3380.

600 Duckworth, O.W., Sposito, G. (2007) Siderophore-promoted dissolution of synthetic and
601 biogenic layer-type Mn oxides. *Chem. Geol.* **242**, 497-508.

602 Dudarev, S.L., Botton, G.A., Savrasov, S.Y., Humphreys, C.J., Sutton, A.P. (1998) Electron-
603 energy-loss spectra and the structural stability of nickel oxide: An LSDA+U study. *Physical*
604 *Review B* **57**, 1505-1509.

605 Franchini, C., Podloucky, R., Paier, J., Marsman, M., Kresse, G. (2007) Ground-state properties
606 of multivalent manganese oxides: Density functional and hybrid density functional calculations.
607 *Physical Review B* **75**, 195128-195111.

608 Fuller, C.C., Bargar, J.R. (2014) Processes of zinc attenuation by biogenic manganese oxides
609 forming in the hyporheic zone of Pinal Creek, Arizona. *Environmental Science and Technology*
610 **48**, 2165-2172.

611 Giovanoli, R., Stahli, E., Feitknecht, W. (1970) Tetravalent manganese oxide hydroxide with
612 stratified lattice. *Helvetica Chimica Acta* **53**, 209-220.

613 Good, N.E., Winget, G.D., Winter, W., Connolly, T.N., Izawa, S., Singh, R.M.M. (1966)
614 Hydrogen ion buffers for biological research. *Biochemistry* **5**, 467-&.

615 Grady, J.K., Chasteen, N.D., Harris, D.C. (1988) Radicals from "Good's" buffers. *Analytical*
616 *Biochemistry* **173**, 111-115.

617 Grangeon, S., Lanson, B., Lanson, M., Manceau, A. (2008) Crystal structure of Ni-sorbed
618 synthetic vernadite: a powder X-ray diffraction study. *Mineralogical Magazine* **72**, 1279-1291.

619 Grangeon, S., Manceau, A., Guilhermet, J., Gaillot, A.-C., Lanson, M., Lanson, B. (2012) Zn
620 sorption modifies dynamically the layer and interlayer structure of vernadite. *Geochim.*
621 *Cosmochim. Acta* **85**, 302-313.

622 Kirsch, M., Lomonosova, E.E., Korth, H.-G., Sustmann, R., de Groot, H. (1998) Hydrogen
623 Peroxide Formation by Reaction of Peroxynitrite with HEPES and Related Tertiary Amines:
624 Implications for a General Mechanism. *Journal of Biological Chemistry* **273**, 12716-12724.

625 Kwon, K.D., Refson, K., Sposito, G. (2010) Surface complexation of Pb(II) by hexagonal
626 birnessite nanoparticles. *Geochim. Cosmochim. Acta* **74**, 6731-6740.

627 Lafferty, B.J., Ginder-Vogel, M., Zhu, M.Q., Livi, K.J.T., Sparks, D.L. (2010) Arsenite
628 oxidation by a poorly crystalline manganese-oxide. 2. Results from X-ray absorption
629 spectroscopy and X-ray diffraction. *Environ. Sci. Technol.* **44**, 8467-8472.

630 Lanson, B., Drits, V.A., Feng, Q., Manceau, A. (2002a) Structure of synthetic Na-birnessite:
631 Evidence for a triclinic one-layer unit cell. *American Mineralogist* **87**, 1662-1671.

632 Lanson, B., Drits, V.A., Gaillot, A.C., Silvester, E., Plancon, A., Manceau, A. (2002b) Structure
633 of heavy-metal sorbed birnessite: Part 1. Results from X-ray diffraction. *American Mineralogist*
634 **87**, 1631-1645.

635 Lanson, B., Marcus, M.A., Fakra, S., Panfili, F., Geoffroy, N., Manceau, A. (2008) Formation of
636 Zn–Ca phyllomanganate nanoparticles in grass roots. *Geochim. Cosmochim. Acta* **72**, 2478-
637 2490.

638 Lingane, J.J., Karplus, R. (1946) New method for determination of manganese. *Industrial and*
639 *Engineering Chemistry-Analytical Edition* **18**, 191-194.

640 Manceau, A., Drits, V.A., Silvester, E., Bartoli, C., Lanson, B. (1997) Structural mechanism of
641 Co^{2+} oxidation by the phyllomanganate buserite. *American Mineralogist* **82**, 1150-1175.

642 Manceau, A., Lanson, B., Drits, V.A. (2002) Structure of heavy metal sorbed birnessite. Part III:
643 Results from powder and polarized extended X-ray absorption fine structure spectroscopy.
644 *Geochim. Cosmochim. Acta* **66**, 2639-2663.

645 Manceau, A., Lanson, M., Geoffroy, N. (2007) Natural speciation of Ni, Zn, Ba, and As in
646 ferromanganese coatings on quartz using X-ray fluorescence, absorption, and diffraction.
647 *Geochim. Cosmochim. Acta* **71**, 95-128.

648 Manceau, A., Marcus, M.A., Grangeon, S., Lanson, M., Lanson, B., Gaillot, A.C.,
649 Skanthakumar, S., Soderholm, L. (2013) Short-range and long-range order of phyllomanganate
650 nanoparticles determined using high-energy X-ray scattering. *Journal of Applied*
651 *Crystallography* **46**, 193-209.

652 Momma, K., Izumi, F. (2011) VESTA 3 for three-dimensional visualization of crystal,
653 volumetric and morphology data. *Journal of Applied Crystallography* **44**, 1272-1276.

654 Murray, J.W. (1975) Interaction of metal-ions at manganese dioxide solution interface.
655 *Geochimica Cosmochimica Acta* **39**, 505-519.

656 Newville, M. (2001) IFEFFIT: interactive XAFS analysis and FEFF fitting. *Journal of*
657 *Synchrotron Radiation* **8**, 322-324.

658 Oh, S.J., Gweon, G.H., Park, J.G. (1992) Origin of 3*s* splitting in the photoemission spectra of
659 Mn and Fe insulating compounds. *Physical Review Letters* **68**, 2850-2853.

660 Peacock, C.L. (2009) Physiochemical controls on the crystal-chemistry of Ni in birnessite:
661 Genetic implications for ferromanganese precipitates. *Geochim. Cosmochim. Acta* **73**, 3568-
662 3578.

663 Peacock, C.L., Sherman, D.M. (2007) Sorption of Ni by birnessite: Equilibrium controls on Ni in
664 seawater. *Chem. Geol.* **238**, 94-106.

665 Peña, J., Kwon, K.D., Refson, K., Bargar, J.R., Sposito, G. (2010) Mechanisms of nickel
666 sorption by a bacteriogenic birnessite. *Geochim. Cosmochim. Acta* **74**, 3076-3089.

667 Perdew, J.P., Burke, K., Ernzerhof, M. (1996) Generalized gradient approximation made simple.
668 *Phys. Rev. Lett.* **77**, 3865-3868.

669 Pfrommer, B.G., Cote, M., Louie, S.G., Cohen, M.L. (1997) Relaxation of crystals with the
670 quasi-Newton method. *J. Comput. Phys.* **131**, 233-240.

671 Post, J.E. (1999) Manganese oxide minerals: Crystal structures and economic and environmental
672 significance. *Proceedings of the National Academy of Sciences of the United States of America*
673 **96**, 3447-3454.

674 Ravel, B., Kelly, S.D. (2007) *The difficult chore of measuring coordination by EXAFS*, in:
675 Hedman, B., Painetta, P. (Eds.), X-Ray Absorption Fine Structure-XAFS13. Amer Inst Physics,
676 Melville, pp. 150-152.

Rehr, J.J., Deleon, J.M., Zabinsky, S.I., Albers, R.C. (1991) Theoretical X-ray absorption fine-structure standards. *Journal of the American Chemical Society* **113**, 5135-5140.

Rollmann, G., Rohrbach, A., Entel, P., Hafner, J. (2004) First-principles calculation of the structure and magnetic phases of hematite. *Physical Review B* **69**, 165107.

Silvester, E., Manceau, A., Drits, V.A. (1997) Structure of synthetic monoclinic Na-rich birnessite and hexagonal birnessite .2. Results from chemical studies and EXAFS spectroscopy. *American Mineralogist* **82**, 962-978.

Sposito, G. (2008) *The chemistry of soils*. Oxford University Press.

Takahashi, Y., Manceau, A., Geoffroy, N., Marcus, M.A., Usui, A. (2007) Chemical and structural control of the partitioning of Co, Ce, and Pb in marine ferromanganese oxides. *Geochim. Cosmochim. Acta* **71**, 984-1008.

Tebo, B.M., Bargar, J.R., Clement, B.G., Dick, G.J., Murray, K.J., Parker, D., Verity, R., Webb, S.M. (2004) Biogenic manganese oxides: Properties and mechanisms of formation. *Annual Review of Earth and Planetary Sciences* **32**, 287-328.

Toner, B., Manceau, A., Webb, S.M., Sposito, G. (2006) Zinc sorption to biogenic hexagonal-birnessite particles within a hydrated bacterial biofilm. *Geochim. Cosmochim. Acta* **70**, 27-43.

Vanderbilt, D. (1990) Soft Self-Consistent Pseudopotentials in a Generalized Eigenvalue Formalism. *Physical Review B* **41**, 7892-7895.

Vetter, K.J., Jaeger, N. (1966) Potentialausbildung an der Mangandioxid-Elektrode als oxidelektrode mit nichtstöchiometrischem oxid. *Electrochimica Acta* **11**, 401-419.

Villalobos, M., Bargar, J., Sposito, G. (2005) Mechanisms of Pb(II) sorption on a biogenic manganese oxide. *Environ. Sci. Technol.* **39**, 569-576.

Villalobos, M., Escobar-Quiroz, I.N., Salazar-Camacho, C. (2014) The influence of particle size and structure on the sorption and oxidation behavior of birnessite: I. Adsorption of As(V) and oxidation of As(III). *Geochim. Cosmochim. Acta* **125**, 564-581.

Villalobos, M., Lanson, B., Manceau, A., Toner, B., Sposito, G. (2006) Structural model for the biogenic Mn oxide produced by Pseudomonas putida. *American Mineralogist* **91**, 489-502.

Villalobos, M., Toner, B., Bargar, J., Sposito, G. (2003) Characterization of the manganese oxide produced by pseudomonas putida strain MnB1. *Geochim. Cosmochim. Acta* **67**, 2649-2662.

Wang, Y., Feng, X., Villalobos, M., Tan, W., Liu, F. (2012) Sorption behavior of heavy metals on birnessite: Relationship with its Mn average oxidation state and implications for types of sorption sites. *Chem. Geol.* **292**, 25-34.

Webb, S.M. (2005) SIXpack: a graphical user interface for XAS analysis using IFEFFIT. *Physica Scripta* **T115**, 1011-1014.

711 Yang, D.S., Wang, M.K. (2001) Syntheses and characterization of well-crystallized birnessite.
712 *Chemistry of Materials* **13**, 2589-2594.

713 Yin, H., Tan, W., Zheng, L., Cui, H., Qiu, G., Liu, F., Feng, X. (2012) Characterization of Ni-
714 rich hexagonal birnessite and its geochemical effects on aqueous Pb^{2+}/Zn^{2+} and As(III).
715 *Geochim. Cosmochim. Acta* **93**, 47-62.

716 Zhao, G., Chasteen, N.D. (2006) Oxidation of Good's buffers by hydrogen peroxide. *Analytical*
717 *Biochemistry* **349**, 262-267.

718 Zhao, W., Cui, H.J., Liu, F., Tan, W.F., Feng, X.H. (2009) Relationship between Pb^{2+} adsorption
719 and average Mn oxidation state in synthetic birnessites. *Clays and Clay Minerals* **57**, 513-520.

720 Zhu, M., Farrow, C.L., Post, J.E., Livi, K.J.T., Billinge, S.J.L., Ginder-Vogel, M., Sparks, D.L.
721 (2012) Structural study of biotic and abiotic poorly-crystalline manganese oxides using atomic
722 pair distribution function analysis. *Geochim. Cosmochim. Acta* **81**, 39-55.

723 Zhu, M., Ginder-Vogel, M., Parikh, S.J., Feng, X.-H., Sparks, D.L. (2010a) Cation effects on the
724 layer structure of biogenic Mn-oxides. *Environ. Sci. Technol.* **44**, 4465-4471.

725 Zhu, M., Ginder-Vogel, M., Sparks, D.L. (2010b) Ni(II) sorption on biogenic Mn-oxides with
726 varying Mn octahedral layer structure. *Environ. Sci. Technol.* **44**, 4472-4478.

727

728

Table 1

Table 1. Physicochemical properties of Mn oxide samples

Sample ID	Specific surface area[a] (m^2/g)	AMON[b]	Na/Mn[c] (mol %)	Water content[d] (%)	Particle size in *ab* plane[e] (nm)
δ-MnO_2	254[f]	4.01 ± 0.05	22.7 ± 0.5	< 20	2 – 4
TcBi	30	3.84 ± 0.04	30.0 ± 0.5	8.9	25 – 50
δ-MnO_2 (pH 6.6; 48 h)	232	3.95 ± 0.05	6.5 ± 0.5	-	-
Mn^{III}_δ-MnO_2 (pH 6.6; 48 h)	200	3.65 ± 0.05	3.0 ± 0.5	-	-

[a] Determined by a 5-point BET N_2(g) adsorption isotherm (Micromeritics Gemini 2375)
[b] **Section 2.3**
[c] Measured by ICP-OES after complete dissolution in 1.5 % HNO_3 and 10 mM oxalic acid
[d] Determined by thermogravimetric analysis (Metler Toledo TG/SDTA 851e)
[e] Determined from transmission electron microscopy (TEM) images
[f] Duckworth and Sposito (2007)

Table 2

Table 2. Samples investigated by EXAFS spectroscopy. Surface loading (q) and concentration of Mn(II) measured in solution (c_{Mn}) are reported for each sample; separate samples were used for AMON determination.

Mineral	Sample ID[a]	EXAFS		AMON		
		q (mol Ni mol^{-1} Mn)	c_{Mn} (μM)	q (mol Ni mol^{-1} Mn)	c_{Mn} (μM)	AMON
δ-MnO_2	δ-MnO_2	-	n.d.[b]	-	n.d.	3.95
	Ni 0.05	0.05	n.d.	0.05	n.d.	3.95
	Ni 0.18	0.18	n.d.	0.18	n.d.	4.01
Mn^{III}_δ-MnO_2	Mn^{III}_δ-MnO_2	-	71.7	-	74.2	3.65
	Ni 0.01	0.01	63.1	0.01	76.8	3.68
	Ni 0.02	0.02	82.1	0.03	87.8	3.70
	Ni 0.04	0.04	120.9	0.06	123.7	3.74
	Ni 0.08	0.08	178.1	0.09	174.8	3.73
TcBi	Ni 0.02	0.02	n.d.	0.02	n.d.	-

[a] The sample ID contains the sorbent name or surface loading in units of mol Ni mol^{-1} Mn.
[b] Not detected

Table 3

Table 3. Summary of EXAFS fitting parameters obtained for δ-MnO_2 samples. Loadings corresponding to CS and ES bonding environments are calculated according to $q_{\text{Ni-CS}} = q * f$ and $q_{\text{Ni-ES}} = q * (1 - f)$, respectively.

Sample	Shell ID[a]	A[b]	R (Å)	σ^2 (Å^2)	ΔE_0 (eV)	Red chi^2	R-factor	f	$q_{\text{Ni-ES}}$/ $q_{\text{Ni-CS}}$
	Ni-O_1	6	2.02±0.01	0.0056±0.0003	-7.66±0.74	0.00	0.0126	0.824±0.024	
	Ni-Mn_1^{ES}	6 * (1 − f)	2.84±0.01	σ^2(Ni-Mn_1^{CS})					0.01/
Ni 0.05	Ni-Mn_1^{CS}	6 * f	3.46±0.01	0.0072±0.0005					0.04
	Ni-O_3	9 * f + 12 * (1 − f)	4.46±0.02	0.0082±0.0021					(±0.01)[c]
	Ni-Mn_2^{CS}	6 * f	5.33±0.01	0.0075±0.0015					
	Ni-O_1	6	2.03±0.01	0.0067±0.0003	-7.10±0.70	0.00	0.0098	0.793±0.042	
	Ni-Mn_1^{ES}	4 * (1 − f)	2.91±0.02	σ^2(Ni-Mn_1^{CS})					0.04/
Ni 0.18	Ni-Mn_1^{CS}	6 * f	3.47±0.01	0.0099±0.0007					0.14
(1)	Ni-O_3	9 * f + 12 * (1 − f)	4.46±0.02	0.0113±0.0023					(±0.03)
	Ni-Mn_2^{CS}	6 * f	5.34±0.02	0.0110±0.0020					
	Ni-O_1	6	2.03±0.01	0.0067±0.0003	-7.12±0.73	0.03	0.0107	0.866±0.028	
	Ni-Mn_1^{ES}	6 * (1 − f)	2.91±0.02	σ^2(Ni-Mn_1^{CS})					0.02
Ni 0.18	Ni-Mn_1^{CS}	5 * f	3.47±0.01	0.0091±0.0006					0.16
(2)	Ni-O_3	9 * f + 12* (1-f)	4.46±0.02	0.0144±0.0035					(±0.03)
	Ni-Mn_2^{CS}	5 * f	5.34±0.02	0.0103±0.0021					
	Nind/Nvar	26/12							

[a] Ni-O and Ni-Mn shell labels follow from Peña et al. (2010); in the text Ni-Mn_1 is referred to as Ni-Mn.
[b] The amplitude (A) of Ni-O and Ni-Mn shells are defined as the product of the CN and a scaling parameter (f), where f refers to the fraction of Ni in the CS geometry and (1 – f) refers to the fraction of Ni in the ES geometry.
[c] the uncertainty in the surface excess q is estimated assuming a 20 % uncertainty in the fraction f.

Table 4

Table 4. EXAFS fitting parameters obtained for TcBi and Mn^{III}_δ-MnO_2 samples. Loadings corresponding to CS and ES bonding environments are calculated according to $q_{CS} = q * f$ and $q_{ES} = q * (1 - f)$, respectively.

Sample	Shell ID[a]	A^b	R (Å)	σ^2 (Å^2)	ΔE_0 (eV)	Red chi^2	R-factor	f	$q_{Ni\text{-}ES}$/ $q_{Ni\text{-}CS}$
Ni 0.02	Ni-O_1	6	2.06±0.01	0.0069±0.0003	-6.62±1.06	0.43	0.0042	-	-
TcBi pH8	Ni-Mn^{DES}	3.21±0.45	3.09±0.01	0.0090±0.0012					
	Ni-O_1	6	2.04±0.01	0.0062±0.0003	-6.08±1.01	13.94	0.0053	0.517±0.263	
Ni 0.01	Ni-Mn_1^{ES}	2 * (1 − f)	3.01±0.03	0.0120±0.0041					0.005
	Ni-Mn_1^{CS}	4 * f	3.48±0.01	0.0073±0.0035					0.005 (±0.003)[c]
	Ni-O_1	6	2.05±0.01	0.0061±0.0004	-5.82±1.26	23.37	0.0087	0.543±0.274	
Ni 0.02	Ni-Mn_1^{ES}	2 * (1 − f)	3.02±0.03	0.0110±0.0046					0.009
	Ni-Mn_1^{CS}	4 * f	3.47±0.01	0.0064±0.0035					0.011 (±0.005)[c]
	Ni-O_1	6	2.04±0.01	0.0063±0.0003	-6.10±1.00	1.42	0.0051	0.608±0.216	
Ni 0.04	Ni-Mn_1^{ES}	2 * (1 − f)	3.02±0.02	0.0095±0.0039					0.016
	Ni-Mn_1^{CS}	4 * f	3.47±0.01	0.0065±0.0024					0.024 (±0.009)[c]
	Ni-O_1	6	2.05±0.01	0.0053±0.0005	-5.79±1.65	0.86	0.0135	0.392±0.294	
Ni 0.08	Ni-Mn_1^{ES}	2 * (1 − f)	3.05±0.03	0.0086±0.0035					0.049
	Ni-Mn_1^{CS}	4 * f	3.47±0.02	0.0055±0.0028					0.031 (±0.024)[c]
	Nind/Nvar		13/6						

[a] Ni-O and Ni-Mn shell labels follow from Peña (2010); in the text Ni-Mn_1 is referred to as Ni-Mn.
[b] The amplitude (A) of Ni-O and Ni-Mn shells are defined as the product of the CN and a scaling parameter (f), where f refers to the fraction of Ni in the CS geometry and $(1 - f)$ refers to the fraction of Ni in the ES geometry.
[c] the uncertainty in the surface excess q is estimated based on the uncertainty in the fraction, f.

Table 5. Interatomic distances (in units of Å) in geometry-optimized Ni DES and DCS surface complexes. Values in < > represent average distances. See **Fig. 2** for bonding configurations of DES and DCS species. The superscript denotes the number of Mn(III) octahedra to which Ni is bonded.

Distance	DES surface complex					DCS surface complex	
	DES_{O2Mn}	$DES_{O2Mn}^{1Mn(III)}$	DES_{O3Mn}	$DES_{O3Mn}^{1Mn(III)}$	$DES_{O3Mn}^{2Mn(III)}$	DCS_0	DCS_H
Ni-O	2.05	2.08	2.04	2.05	2.09	2.01	2.01
	2.06	2.03	2.05	2.06	2.00	2.02	2.00
	2.00	2.00	2.03	2.03	2.03	2.08	2.17
	2.10	2.12	2.15	2.12	2.12	2.15	2.16
	2.18	2.20	2.13	2.16	2.17	2.18	2.15
	2.14	2.13	2.12	2.12	2.19	2.21	2.17
	<2.09>	<2.10>	<2.08>	<2.09>	<2.10>	<2.11>	<2.11>
Ni-Mn	2.90	2.90	2.98	2.98	3.01	3.44	3.44
	2.88	2.91	2.96	3.00	3.10	3.45	3.45
	<2.89>	<2.91>	<2.97>	<2.99>	<3.05>	<3.45>	<3.45>

Figure captions

Fig. 1. Schematic representations of Ni-birnessite surface complexes: Ni = black, Mn octahedra = hatched, O = grey. The ideal coordination number (*CN*) and interatomic distance between Ni and Mn [R(Ni-Mn)] for each surface complex geometry is included below each cartoon, where TCS (**a**) refers to a triple-corner-sharing complex wherein a metal cation binds to the three doubly-coordinated oxygen atoms surrounding a vacancy site; INC (**b**) refers to the incorporation of a metal cation into a vacancy in the MnO_2 sheet; DCS (**c**) refers to a double-corner-sharing complex where a metal cation binds to two singly-coordinated oxygen atoms at the particle edges; DES (**d**) refers to a double-edge-sharing complex wherein a metal cation binds to two singly- and one doubly-coordinated oxygen atoms at the particle edges.

Fig. 2. Structures of geometry-optimized Ni surface complexes. Color scheme: blue = Ni; grey = Mn; red = O; pink = H. In DES_{O2Mn}, Ni binds with O_{2Mn} and two $O_{1Mn.}$ In DES_{O3Mn}, Ni binds with O_{3Mn} and two O_{1Mn}. The $DES_{O3Mn}^{2Mn(III)}$ structure is like DES_{O3Mn} with Ni bound to two Mn(III) octahedra. The ES structure has three Mn atoms, while DES has two Mn atoms in the first Ni-Mn coordination shell. In DCS_0, the O_{2Mn} is deprotonated, while in DCS_H it is protonated.

Fig. 3. Sorption isotherms of Ni on δ-MnO_2 (triangles) and Mn^{III}_δ-MnO_2 (circles) measured at pH 6.6. The lines are intended to guide the eye. Samples investigated by EXAFS spectroscopy are indicated by filled symbols.

Fig. 4. Ni K-edge EXAFS spectra and corresponding Fourier transforms for Ni adsorbed by δ-MnO_2 (**Table 2** and **Table 3**).

Fig. 5. Ni K-edge EXAFS spectra and corresponding Fourier transforms for Ni adsorbed by Mn^{III}_δ-MnO_2 and TcBi (**Table 2** and **Table 4**).

Figure 1

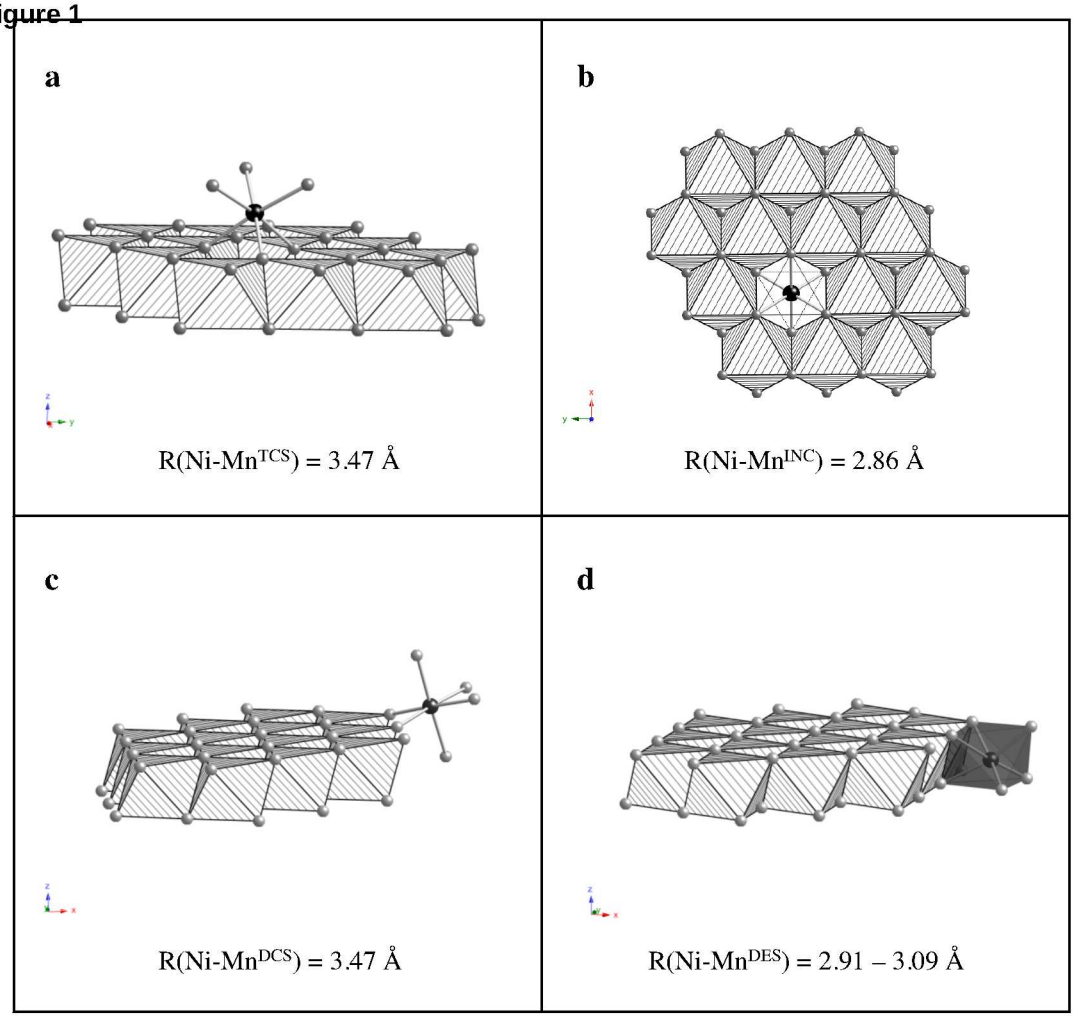
a
b
c
d
R(Ni-Mn^TCS) = 3.47 Å
R(Ni-Mn^INC) = 2.86 Å
R(Ni-Mn^DCS) = 3.47 Å
R(Ni-Mn^DES) = 2.91 – 3.09 Å

Figure 2

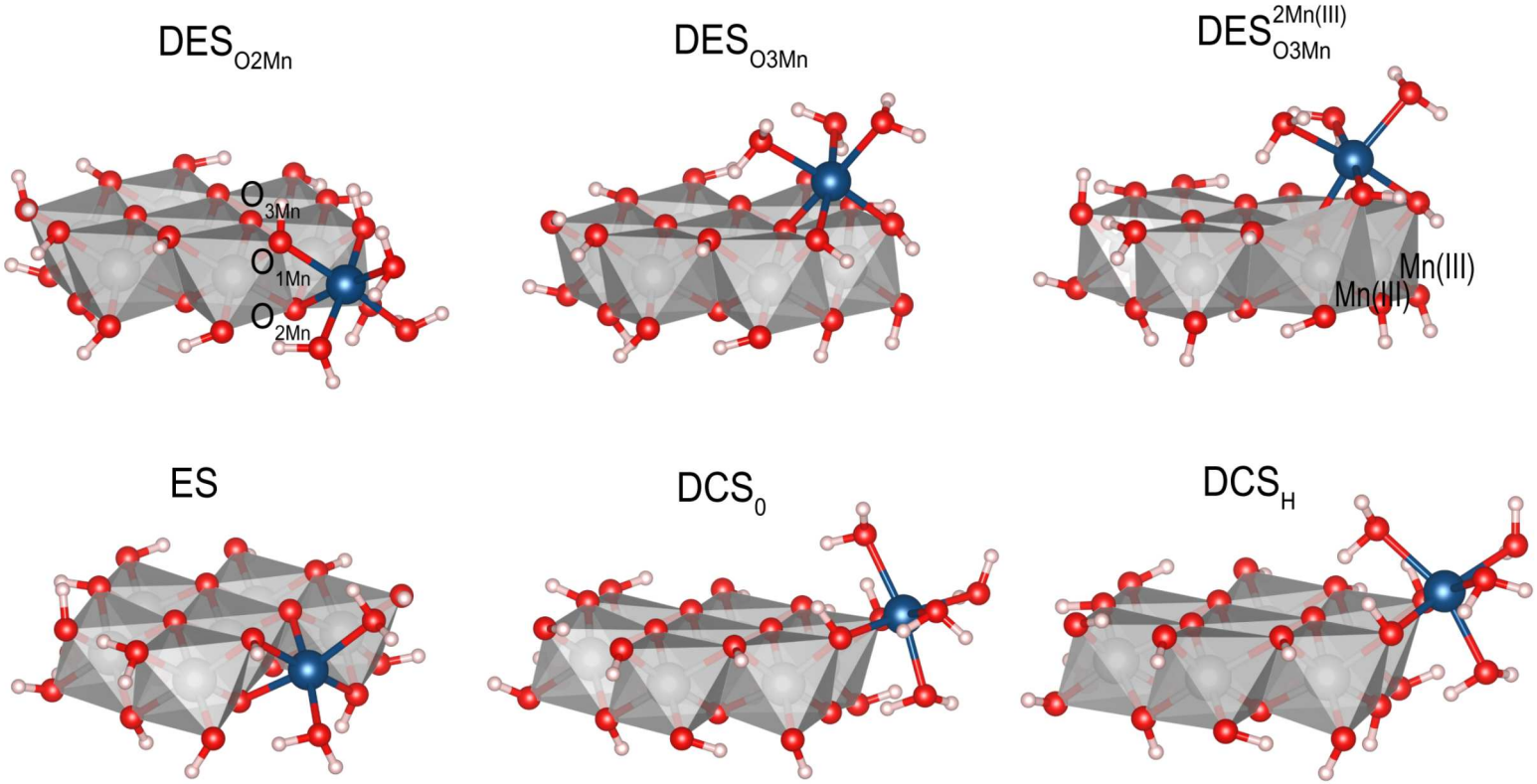
DES O2Mn
O 3Mn
O 1Mn
O 2Mn
DES O3Mn
DES 2Mn(III) O3Mn
Mn(III)
Mn(III)
ES
DCS 0
DCS H

Figure 3

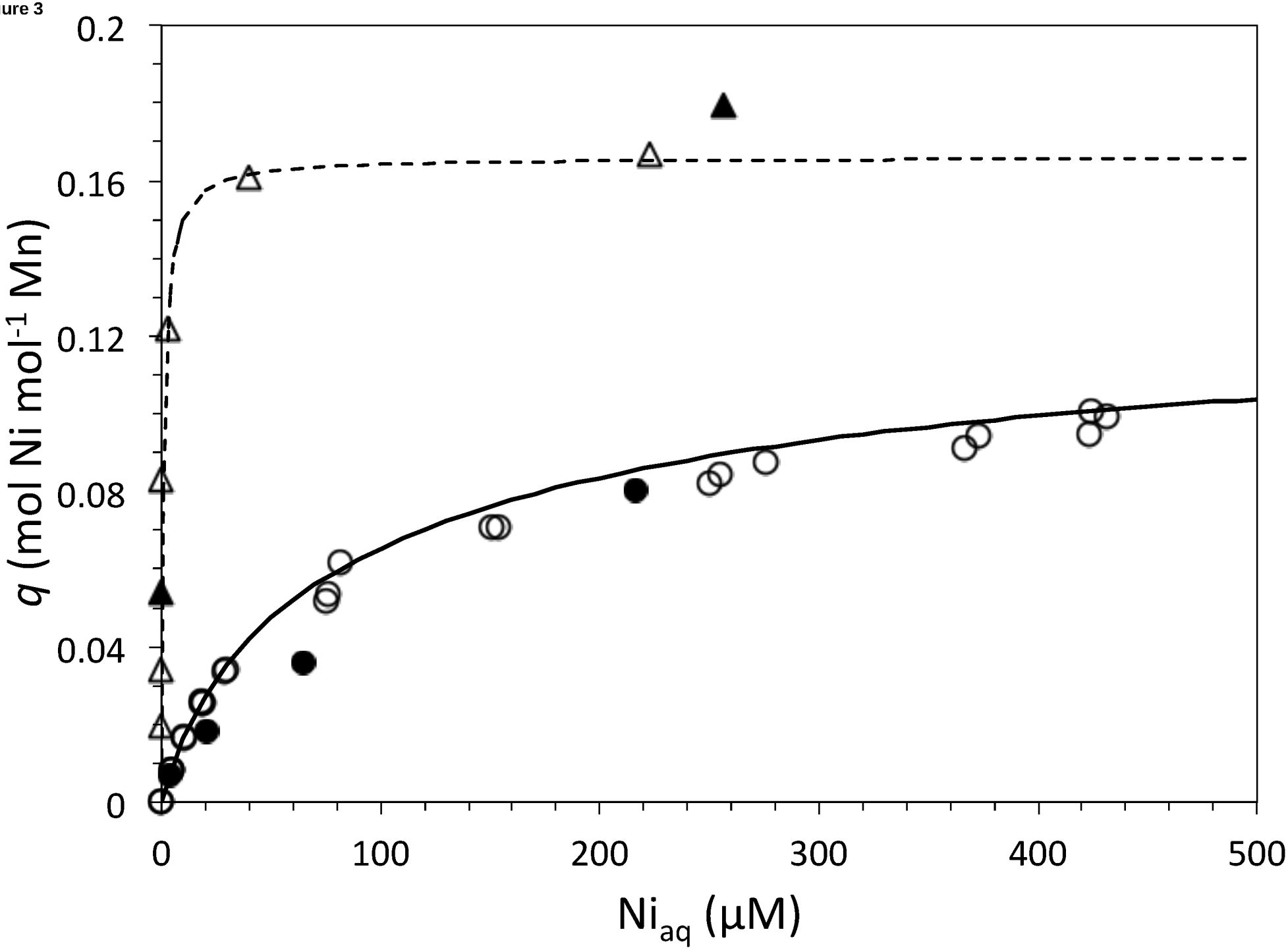

Figure 4

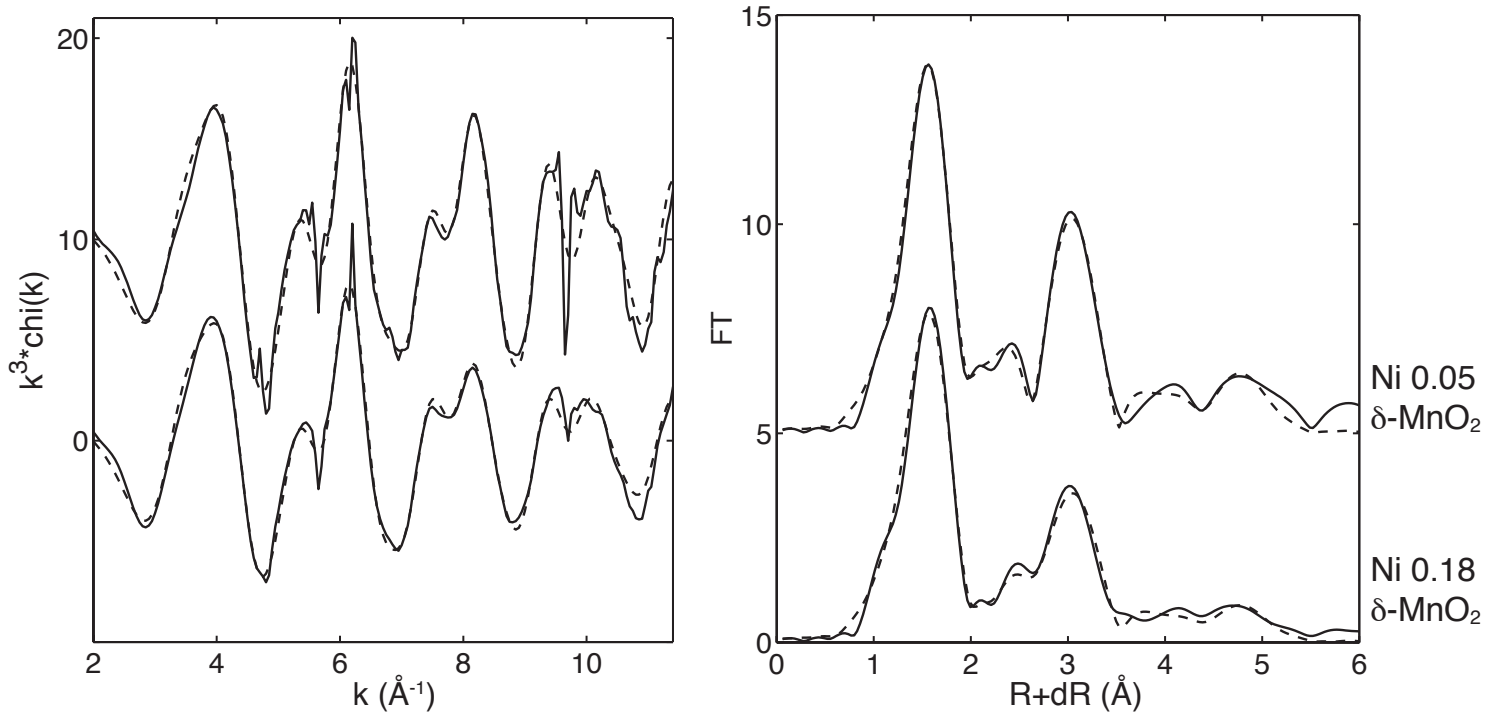
20
10
0
k^3*chi(k)
2
4
6
8
10
k (Å^{-1})
15
10
5
0
FT
0
1
2
3
4
5
6
R+dR (Å)
Ni 0.05
δ-MnO_2
Ni 0.18
δ-MnO_2

Figure 5

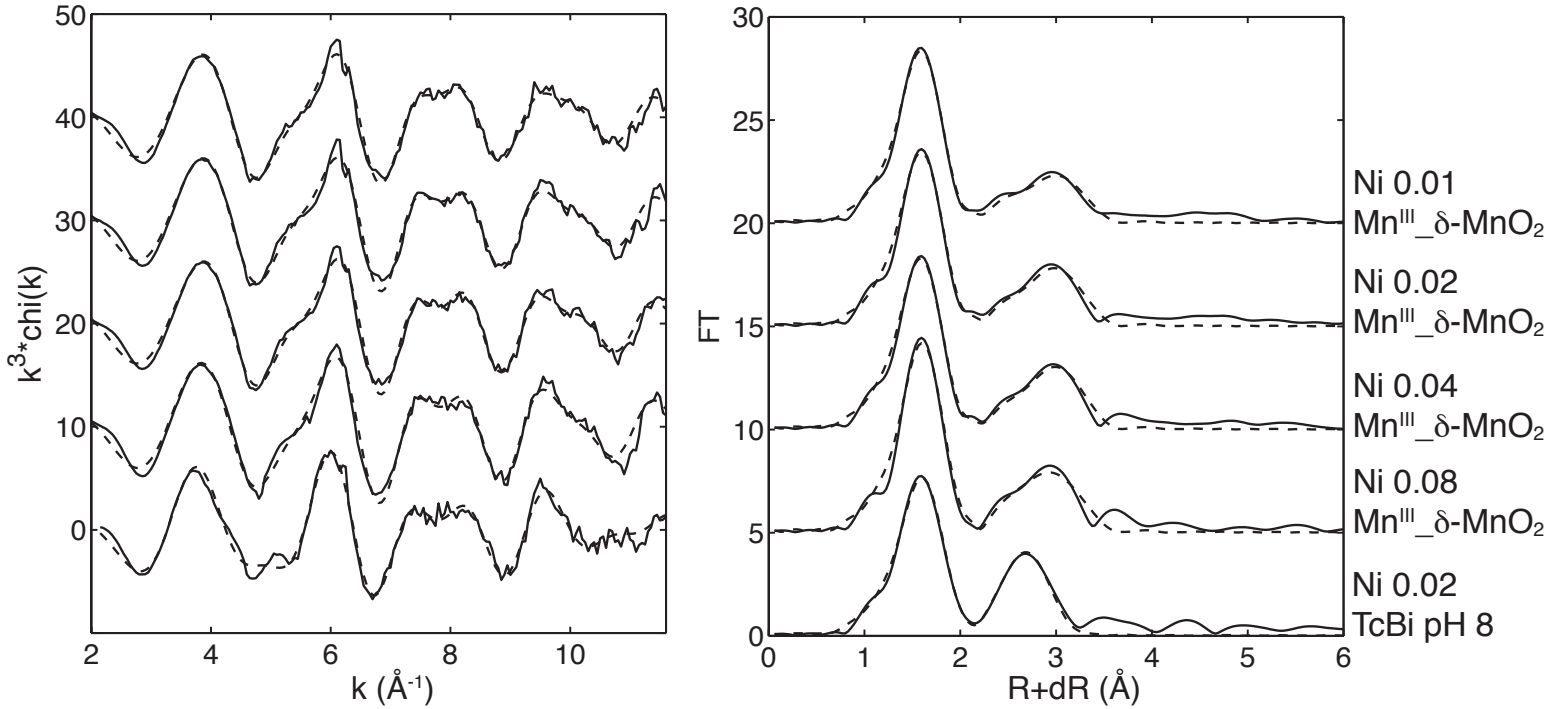
k³*chi(k)
k (Å⁻¹)
FT
R+dR (Å)
Ni 0.01
Mn^III_δ-MnO2
Ni 0.02
Mn^III_δ-MnO2
Ni 0.04
Mn^III_δ-MnO2
Ni 0.08
Mn^III_δ-MnO2
Ni 0.02
TcBi pH 8

Revised manuscript with tracked changes

Click here to download Appendix: Simanova_Pena_Text_revised_tracked_changes.pdf

Electronic Annex

Click here to download Electronic Annex: Simanova_Pena_EA_revised.docx